Acta Polytechnica CTU Proceedings **50**:88–93, 2024
https://doi.org/10.14311/APP.2024.50.0088

Published by the Czech Technical University in Prague

OPTIMIZATION OF FIB MILLING PROCEDURE FOR MICROMECHANICAL TESTING OF CEMENT PASTES

Jan Procházka[a,*], Jiří Němeček [1,b], Patricie Halodová[a], Jiří Němeček [2,b]

[a] *Research centre Řež, Hlavní 130, Řež, 250 68 Husinec, Czech Republic*

[b] *Czech Technical University in Prague, Faculty of Civil Engineering, Thákurova 7, 166 29 Prague 6 – Dejvice, Czech Republic*

[*] corresponding author: jan.prochazka@cvrez.cz

Abstract. This study focuses on optimizing the Focused Ion Beam (FIB) preparation process for micro-beams made from cement paste prepared from Portland cement CEM I-42.5R, which includes four phases: inner and outer products, Portlandite, and residual clinker. The effects of the primary electron beam, focused ion beam, image drift, imaging issues, and sample moisture cycling were investigated. Recommendations on specific fabrication procedures and FIB milling parameters, such as accelerating voltage, probe current, and time, were provided.

Keywords: Cement paste, focused ion beam, nanoindentation, micro-beam, C–S–H gel, scanning electron microscopy.

1. Introduction

Ordinary cement paste is a heterogeneous material, primarily composed of Calcium-Silica-Hydrate (C–S–H) gel, Portlandite (CH), residual clinker (C), porosity, and other minor phases. The C–S–H gel exists in two variants with different densities. Low-density C–S–H gel, along with other minor phases, forms the outer product (OP), while high-density C–S–H gel, also with other minor phases, forms the inner product (IP) [1, 2]. These phases exhibit variable chemical compositions and different mechanical properties. Nanoindentation can be used to assess the mechanical properties, such as the Young's modulus or hardness of these micrometer-sized phases [3–5].

However, nanoindentation cannot directly measure the compressive and tensile strengths or fracture energy of these phases. These properties can be determined by fabricating micro-pillars or micro-beams using focused ion beam (FIB) techniques. Subsequently, compressing the micro-pillars [6, 7] or bending the micro-beams [8, 9] with a nanoindenter can be used to derive the elastic and fracture properties of the individual phases. Despite the indisputable advantages of the FIB milling technique, several potential undesirable effects associated with ion beam nanofabrication, such as temperature-induced phase transformations, gallium implantation, and unintended material redeposition, can significantly influence the measurement results [9].

Therefore, when using an ion beam for micro-beam fabrication, it is essential to select appropriate sputtering parameters to minimize the impact of nanofabrication on the mechanical testing results. This study elucidates the crucial steps involved in preparing micro-beams using FIB techniques and discusses the utilization of optimized parameters to ensure the efficacy and accuracy of both the manufacturing process and subsequent nanomechanical testing.

2. Materials and methods

2.1. Material

The cement paste samples were mixed from Portland cement CEM I-42.R (Českomoravský cement, Czech Republic) of the chemical composition shown in Table 1 without chemical admixtures and the water-to-cement ratio of 0.4. A fresh paste was cast in cylindrical molds (27 mm in diameter, 70 mm in height) and vibrated to avoid excessive air voids in the structure. Then, the samples were stored in lime water for 20 months. Detailed procedure and sample labeling are described in [10].

2.2. Sample preparation

After the curing period in lime water, the samples were dried at 50 °C for 3 days. Then, the samples were ground for 1 min on SiC paper grit 2 000 and for 2.5 min on SiC paper grit 4 000 with no lubrication. The debris was continuously swept away from the papers throughout the grinding procedure. Final polishing took place on a soft cloth with alcohol-based diamond suspensions for 15 seconds with 0.25 µm grains. The samples were ultrasonically cleaned in an alcohol bath for 1 min after each polishing step [2].

After the polishing, three coarse base-defining marks were engraved in the corners of the analyzed fragment using a diamond tip.

[1] Postdoctoral researcher at Czech Technical University in Prague, ORCID: 0000-0002-5635-695X.

[2] Professor at Czech Technical University in Prague, ORCID: 0000-0002-3565-8182.

Component	CaO	SiO_2	Al_2O_3	Fe_2O_3	MgO	Na_2O	K_2O	SO_3	MnO
CEM I (wt. %)	63.77	20.51	4.74	3.30	1.05	0.15	0.95	3.07	0.09

TABLE 1. Chemical composition of the used Portland cement (XRF data supplied by the manufacturer).

Process step	Label deposition	Trench milling	Rough undercut	Fine polishing	Shortening
Pattern	Lines Text	Stairs rectangles	Polishing rectangle	Polishing rectangles	Polishing rectangle
Dimensions (µm)	$175 \times 45 \times 0.1$	$25 \times 15 \times 15$	$24 \times 15 \times 15$	$20 \times 3 \times 10$ $3 \times 2 \times 10$	$8 \times 5 \times 10$
I_B (pA)	~ 200	$\sim 1\,000$	$\sim 1\,000$	~ 600	~ 600
t_s (min)		~ 240	$2\times \sim 120$	$2\times \sim 90$	~ 10
θ_e (°)	55	55	23	23	55 / 23
θ_B (°)	0	0	32	32	0 / 32

TABLE 2. Recommended FIB parameters and estimated process times for different steps in micro-beam preparation routine.

2.3. IMAGINING AND ION MACHINING

Polished samples were glued to the SEM stub using colloidal silver lacquer (Agar Scientific), and the same lacquer was applied to the sides of the samples to reduce charging.

The location of the four main hydration phases (OP, IP, CH, and C) with large enough dimensions suitable for micro-beam fabrication were identified using a Scanning electron microscope (SEM) Phenom XL Desktop SEM and back-scatter electron (BSE) detector. Also, the coordinates of locations and base-defining marks were recorded for further aid.

The micro-beams and labels for nanoindentation tests were prepared using a dual-beam FIB-SEM Tescan Lyra3 GMU, equipped with Ga^+ COBRA FIB column tilted 55° to the electron column and gas injection system with platinum, tungsten, and carbon precursors for ion-beam assisted deposition (IBAD). The microscope is equipped with external and in-beam detectors for both BSE and secondary electrons (SE).

5-degree-of-freedom stage allows sample positioning with adjustable tilt around axis perpendicullar to both electon and ion beams and (actual) rotation around axis perpendicullar to the sample surface. The controlling system allows software adjustments of image shift and (apparent) rotation. The image is not deformed by apparent rotation only if the sample is perpedicullar to the beam used.

At first, the coarse base-defining marks were made with two platinum alignment tags: one located inside the scratch mark, labeled as coarse, and one on the polished surface, labeled as fine. This set of three base-defining marks allows easier beam positioning using microscopes ranging from optical microscopes to SEMs.

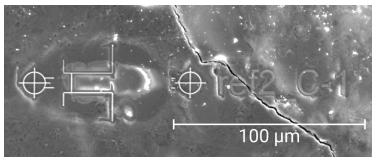

(a) SE

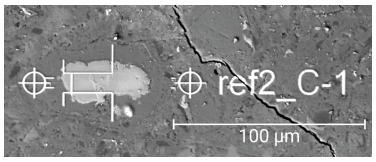

(b) BSE

FIGURE 1. SEM images of the label, alignment tags, and outline for the beam in residual clinker using (a) SE and (b) BSE detectors.

2.4. MICRO-BEAMS

After the marking, the regions of interest were identified and labeled using platinum IBAD. Additional beam outlines and alignment tags were added for easier and more precise ion milling routines, see Figure 1.

The positioning and orientation of a cantilever must allow enough room for nanoindentation measurement of the selected phase in the proximity of the cantilever root. The root shall be as far as possible from phase interfaces too. The desired dimensions of the final equilateral triangular cantilever for testing are 20×8 µm.

The process of cantilever preparation is divided in four steps: high-current trench milling, high-current rough cantilever undercut, low-current cantilever sidewall and cantilever base polishing, and low-current cantilever shortening. Recommended parameters and estimated process times are listed in Table 2.

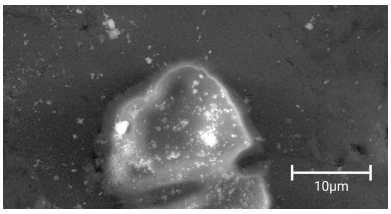

(a) SE, perpendicular to the electron beam.

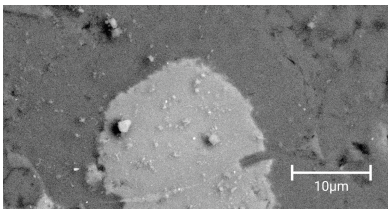

(b) BSE, perpendicular to the electron beam.

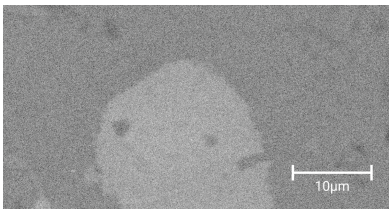

(c) In-Beam BSE, perpendicullar to the electron beam.

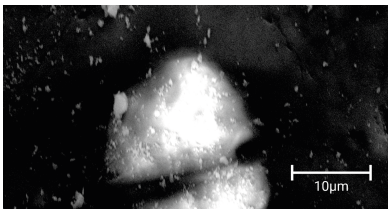

(d) SE, perpendicular to the ion beam.

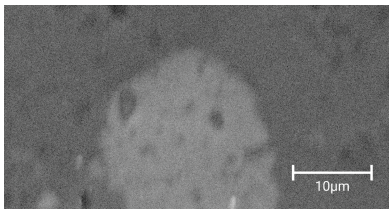

(e) In-Beam BSE, perpendicular to the ion beam.

Figure 2. Comparison of SEM images of residual clinker grain with the sample surface (a–c) perpendicular to electon beam and tilted to the ion beam, and (d–e) tilted to the electron beam and perpendicular to the ion beam, using different detectors (a) SE, (b) In-beam BSE.

3. Results and Discussion

3.1. Imaging issues

As the cement paste is poorly conductive in a vacuum chamber, surface charging is an issue for SEM imaging using SE because the charged surface has a higher secondary electron emission rate as shown in Figures 2(a) and 2(d) due to the negative charge build-up on the scanned surface. BSE imaging is less affected by immediate surface charge, see Figure 2(b), because the detector collects the signal from electrons interacting elastically with the sample surface. Due to their higher energy, BSEs are less susceptible to deflection by the electric fields caused by surface charging. In-chamber BSE detectors have better signal than their in-beam (IB) counterparts that are located inside the SEM column, see Figures 2(b) and 2(c). On the other hand, In-chamber detectors are prone to mechanical damage and cannot be used with tilted specimens during ion fabrication.

In cases where the sample was tilted for FIB processes or cross-section documentation, a combination of the SE detector, primarily for focusing, and the in-beam BSE detector, providing phase and chemical contrast, was used. Otherwise, the in-chamber BSE detector was used.

3.2. Effect of primary electron beam

Continual SEM scanning loads the entire surface of the sample in the view field. In the case of a cementitious sample, the energy deposited by the incident electron beam on the surface cannot dissipate through the material, leading to energy absorption and subsequent thermal effects, such as localized heat damage of the surface. The amount of heat generated depends on the current of the electron beam, and the actual temperature rise depends on several factors, including exposure time, thermal conductivity, heat capacity, and the geometry of the sample [11].

BI	$d_{\mathrm{E,R}}$ (nm)	$d_{\mathrm{E,D}}$ (nm)	I_{E} (pA)
1	7.8	13	∼ 9
2	7.4	12	∼ 11
3	6.6	11	∼ 20
4	6.3	11	∼ 24
5	5.9	10	∼ 35
6	5.4	9.3	∼ 50
7	5.0	8.5	∼ 67
8	4.6	7.8	∼ 95
9	4.5	7.2	∼ 130
10	4.6	6.6	∼ 190
11	5.3	6.1	∼ 270
12	6.9	5.7	∼ 330
13	10	5.5	∼ 450
14	15	5.6	∼ 550
15	24	6.1	∼ 750
16	37	7.4	∼ 880
17	62	11	∼ 1 000

Table 3. Electron beam current I_{B} and spot sizes d_{B} for resolution-optimised (-R) and focal-depth-optimised (-D) scanning modes, respectively, with acceleration voltage of 15 keV.

The microscope used in the study offers two beam-focusing setups optimized for improved resolution or enhanced depth of focus. Differences between estimated spot sizes d_{E} of both modes and beam current I_{E} for beam intensity (BI) indices are listed in Table 3.

Figure 3(a) shows the micro-beam prepared under continuous electron imaging with electron beam intensity BI 17 overheating the sample surface. Electron

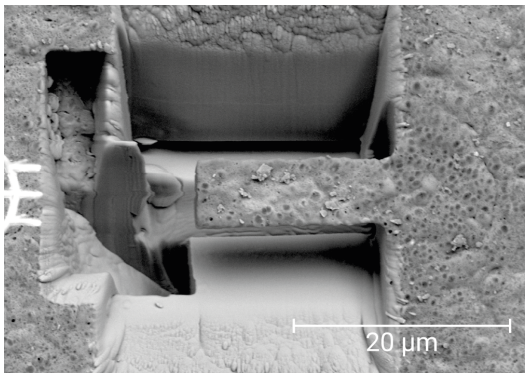

(a) Damaged micro-beam prepared in IP under continuous electron imaging.

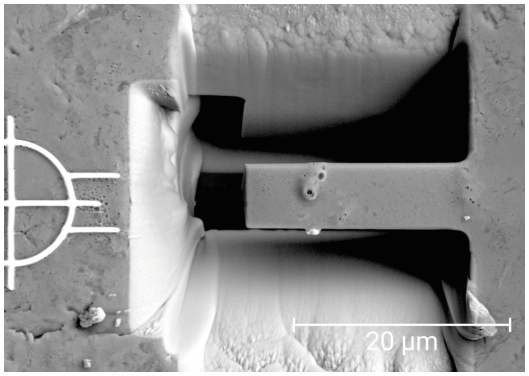

(b) Micro-beam prepared in IP with electron imaging deactivated.

FIGURE 3. Comparison of micro-beams damaged and undamaged by extensive electron beam heating.

imaging using *BI* 7 and deactivating the continuous acquisition during the FIB process minimizes the surface degradation, see Figure 3(b).

BI 7 with pixel dwell time of 3.2 µs and resolution of 512×512 px offers an acceptable compromise between low sample heat loading and reasonable preview image quality. To suppress the surface heat loading even further, the continuous image acquisition should be turned off during FIB processes.

3.3. Effect of ion beam

The FIB, as well as the electron beam or laser beam, is assumed to be elliptical in the plane perpendicular to the beam with a Gaussian-type power profile. As the beam current is defined by masking the defocused beam in the column, the different current settings lead to different standard deviations of the power profile. A higher standard deviation results in blunter edges for higher current ratings. Figure 4 shows four identical ion beam etching routines of rectangular object, 1 µm wide, 8 µm long and deep, in Portlandite using four different FIB presets defined in Table 4. It is clearly seen that with higher beam currents, the edges of the etched objects are less defined and blunter compared to those prepared using lower beam currents. As described in [12], higher current ratings lead to higher temperature rises and broader heated volumes.

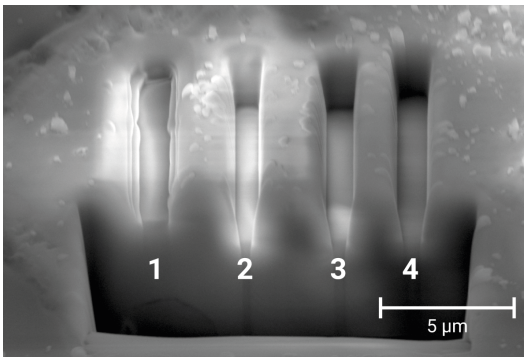

FIGURE 4. Comparison of FIB etching routines performed with different ion beam presets.

Preset	d_A (µm)	d_B (nm)	I_B (pA)	t_s (min)
1	500	130.1	∼ 7 000	0:20
2	200	109.6	∼ 1 000	2:13
3	150	118.2	∼ 600	4:09
4	90	121.9	∼ 200	13:33

TABLE 4. FIB preset parameters for ion acceleration voltage of 30 keV and time needed for etching 1 µm wide, 8 µm long and deep rectangular trench in Portlandite.

In the case of micro-beams prepared in cement paste phases, both effects contribute to artifacts created on the sides of the micro-beam and the base. The Gaussian beam broadening primarily causes blunt edges, while beam-induced heating can lead to geometrical changes in the micro-beam due to possible phase transformations, decomposition, or the release of adsorbed gel water in C-S-H products, resulting in shrinkage and microcracking [9].

Figure 5(a) shows preparation of a micro-beam in Portlandite interrupted after the second stage of rough undercut using the $I_B \sim 7$ nA because of excessive heat loading induced by the FIB. Reducing the beam current to $I_B \sim 1$ nA eliminated the excessive heat loading, see Figure 5(b).

3.4. Effect of image drift

Because of the low conductivity of cement paste in the vacuum chamber, the accumulation of positive charge due to Ga^+ ion implantation and secondary electron emission during the Ga^+ ion beam fabrication can lead to significant charging effects, causing apparent image movement called image drift. This effect can be mitigated by drift correction, where the milling/polishing routine is automatically paused and the reference area is scanned to estimate corrections. The FIB/SEM used in this study allows for either finer pattern correction, where the FIB schedule pattern coordinates are altered for the compensation, or coarser but wider-range image shift correction, where the FIB image shift is adjusted for compensation.

In the case of cement pastes, the period between correction scans had to be reduced to 30–60 seconds. Even though the wider-range correction method of

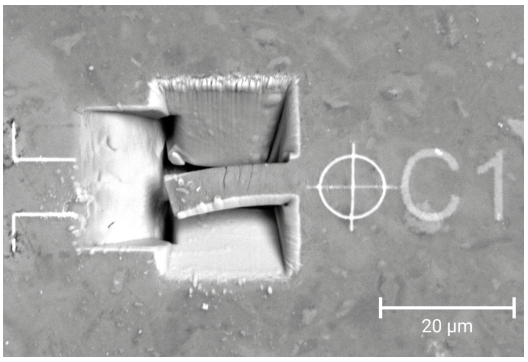

(a) Micro-beam undercut performed using $I_B \sim 7$ nA

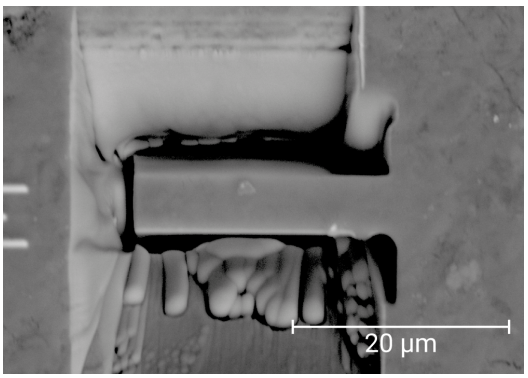

(b) Micro-beam undercut performed using $I_B \sim 1$ nA

Figure 5. Comparison of micro-beams undercut prepared in Portlandite using ion beam current of (a) 7 nA and (b) 1 nA.

image shift was used, it could not always compensate for the drift. In such cases, additional polishing steps were added to achieve the desired micro-beam geometry. See Figure 6(a).

3.5. Effect of moisture cycling

Hydration and dehydration processes in C–S–H gel are associated with volumetric and mechanical changes in the gel [13]. The changes of water partial pressure in the sample between the storage in the given atmosphere and micro-beam preparation in the SEM evacuated chamber induce high artificial stress in the samples, see Figure 7. It was found that week-long storage of the samples in the vacuum of SEM ($p \sim 10^{-6}$ Pa) causes significantly fewer cracks in the samples than atmospheric storage overnight between FIB procedures. Attention must be given to this effect when transporting ready-made micro-beams for nanoindentation testing to another laboratory. We recommend transporting and storing samples in a vacuum to mitigate potential issues.

4. Conclusions

The preparation of micro-beams in cement paste is a time-consuming process with a significant failure rate. During the preparation of beams for nanoindentation testing using FIB techniques, several critical parameters require careful assessment to ensure the

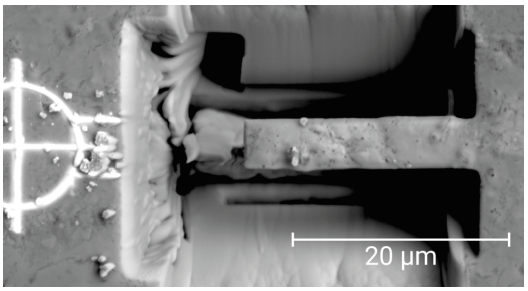

(a) Micro-beam in OP phase recovered by additional polishing.

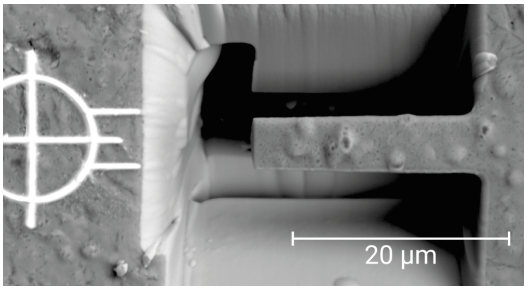

(b) Micro-beam prepared in IP phase.

Figure 6. Comparison of micro-beams (a) affected and (b) not affected by excessive sample drift.

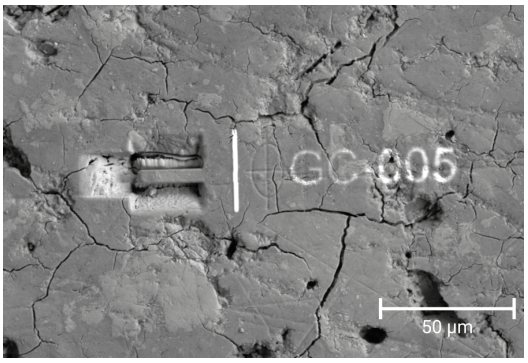

Figure 7. Sample surface damaged by moisture cycling.

procedure's success. The general recommendations are given as:

- Parameters *BI* 7 of the electron beam equal to electron current $I_e \sim 70$ pA combined with higher-gain SE and in-beam BSE detectors are suitable to use to avoid surface overheating and to ensure reasonable image quality. Additionally, continuous image acquisition should be turned off during the FIB milling for the same reason.
- High currents used during FIB milling can lead to excessive heat loading of the sample, resulting in phase transformation, visible bubbles or cracks on the micro-beam, or even geometry changes. Safe current values for different milling steps of Portlandite are provided in Table 2.
- To avoid image drift caused by charging due to the accumulation of Ga^+ ions during FIB fabrication,

it is recommended to perform drift correction by rescanning the measured area at intervals of 30 to 60 seconds.

- Cyclic water resaturation of the cement paste can lead to the creation of a significant number of micro-cracks, potentially damaging already fabricated micro-beams. Therefore, it is advisable to maintain the sample under vacuum conditions throughout the preparation and testing phases to effectively mitigate these effects.

List of symbols

BI Beam Intensity index

BSE Back Scattered Electron (detector)

d_B Ion Beam estimated spot size [nm]

d_E Electron Beam estimated spot size [nm]

FIB Focused Ion Beam

I_B Ion Beam current [A]

I_E Electron Beam current [A]

IBAD Ion Beam Assisted chemical vapour Deposition

SE Secondary Electron (detector)

SEM Scanning Electron Microscope

t_s estimated process time for given beam preparation step [min]

θ_e Sample tilt angle respective to the electron beam [°]

θ_B Sample tilt angle respective to the ion beam [°]

C Residual Clinker

C–S–H Calcium – Silicate – Hydrates

CH Portlandite

IP Inner Product

OP Outer Product

Acknowledgements

This work was financially supported by the project of the Czech Science Foundation grant number 23-05435S.

The presented results were obtained using the CICRR infrastructure, which is financially supported by the Ministry of Education and Culture – project LM2023041.

References

[1] K. L. Scrivener. Backscattered electron imaging of cementitious microstructures: understanding and quantification. *Cement and Concrete Composites* **26**(8):935–945, 2004. https://doi.org/10.1016/j.cemconcomp.2004.02.029

[2] J. Němeček, J. Lukeš, J. Němeček. High-speed mechanical mapping of blended cement pastes and its comparison with standard modes of nanoindentation. *Materials Today Communications* **23**:100806, 2020. https://doi.org/10.1016/j.mtcomm.2019.100806

[3] W. C. Oliver, G. M. Pharr. An improved technique for determining hardness and elastic modulus using load and displacement sensing indentation experiments. *Journal of Materials Research* **7**(6):1564–1583, 1992. https://doi.org/10.1557/JMR.1992.1564

[4] C. Hu, Z. Li. A review on the mechanical properties of cement-based materials measured by nanoindentation. *Construction and Building Materials* **90**:80–90, 2015. https://doi.org/10.1016/j.conbuildmat.2015.05.008

[5] Z. Luo, W. Li, K. Wang, S. P. Shah. Research progress in advanced nanomechanical characterization of cement-based materials. *Cement and Concrete Composites* **94**:277–295, 2018. https://doi.org/10.1016/j.cemconcomp.2018.09.016

[6] R. Shahrin, C. P. Bobko. Micropillar compression investigation of size effect on microscale strength and failure mechanism of Calcium-Silicate-Hydrates (C-S-H) in cement paste. *Cement and Concrete Research* **125**:105863, 2019. https://doi.org/10.1016/j.cemconres.2019.105863

[7] C. Puttbach, G. S. Prinz, C. D. Murray. Strength and stiffness characterization of ultra-high performance concrete (UHPC) cement paste phases through in-situ micro-mechanical testing. *Cement and Concrete Composites* **149**:105520, 2024. https://doi.org/10.1016/j.cemconcomp.2024.105520

[8] J. Němeček, V. Králík, V. Šmilauer, et al. Tensile strength of hydrated cement paste phases assessed by micro-bending tests and nanoindentation. *Cement and Concrete Composites* **73**:164–173, 2016. https://doi.org/10.1016/j.cemconcomp.2016.07.010

[9] J. Němeček, J. Maňák, J. Němeček, T. Krejčí. Effect of vacuum and Focused Ion Beam generated heat on fracture properties of hydrated cement paste. *Cement and Concrete Composites* **100**:139–149, 2019. https://doi.org/10.1016/j.cemconcomp.2019.03.027

[10] J. Němeček, P. Trávníček, M. Keppert, et al. Nanomechanical analysis of Gamma-irradiated cement paste exposed to different humidities. *Construction and Building Materials* **393**:131969, 2023. https://doi.org/10.1016/j.conbuildmat.2023.131969

[11] J. Goldstein. *Scanning Electron Microscopy and X-Ray Microanalysis: A Text for Biologists, Materials Scientists, and Geologists*. Springer US, 1981.

[12] T. Ishitani, H. Kaga. Calculation of local temperature rise in focused-ion-beam sample preparation. *Journal of Electron Microscopy* **44**(5):331–336, 1995. https://doi.org/10.1093/oxfordjournals.jmicro.a051185

[13] M. B. Pinson, E. Masoero, P. A. Bonnaud, et al. Hysteresis from multiscale porosity: modeling water sorption and shrinkage in cement paste. *Physical Review Applied* **3**(6):064009, 2015. https://doi.org/10.1103/PhysRevApplied.3.064009